The Coplane Analysis Technique for Three-Dimensional Wind Retrieval Using the HIWRAP Airborne Doppler Radar

ANTHONY C. DIDLAKE JR.

NASA Goddard Space Flight Center, Greenbelt, Maryland, and Oak Ridge Associated Universities, Oak Ridge, Tennessee

GERALD M. HEYMSFIELD

NASA Goddard Space Flight Center, Greenbelt, Maryland

LIN TIAN

NASA Goddard Space Flight Center, Greenbelt, and Morgan State University/Goddard Earth Sciences Technology and Research Program, Baltimore, Maryland

STEPHEN R. GUIMOND

NASA Goddard Space Flight Center, Greenbelt, and University of Maryland/Earth System Science Interdisciplinary Center, College Park, Maryland

(Manuscript received 8 August 2014, in final form 12 November 2014)

ABSTRACT

The coplane analysis technique for mapping the three-dimensional wind field of precipitating systems is applied to the NASA High-Altitude Wind and Rain Airborne Profiler (HIWRAP). HIWRAP is a dual-frequency Doppler radar system with two downward-pointing and conically scanning beams. The coplane technique interpolates radar measurements onto a natural coordinate frame, directly solves for two wind components, and integrates the mass continuity equation to retrieve the unobserved third wind component. This technique is tested using a model simulation of a hurricane and compared with a global optimization retrieval. The coplane method produced lower errors for the cross-track and vertical wind components, while the global optimization method produced lower errors for the along-track wind component. Cross-track and vertical wind errors were dependent upon the accuracy of the estimated boundary condition winds near the surface and at nadir, which were derived by making certain assumptions about the vertical velocity field. The coplane technique was then applied successfully to HIWRAP observations of Hurricane Ingrid (2013). Unlike the global optimization method, the coplane analysis allows for a transparent connection between the radar observations and specific analysis results. With this ability, small-scale features can be analyzed more adequately and erroneous radar measurements can be identified more easily.

1. Introduction

The use of airborne Doppler radars has significantly advanced our understanding of meteorological phenomena by providing wind structure information that details the dynamics of an evolving system. Airborne platforms have been particularly important for observing phenomena that occur in remote areas, such as tropical cyclones over the open ocean. Lhermitte (1971) first discussed the idea of using airborne Doppler radars for obtaining three-dimensional wind structures. A single Doppler radar beam measures the along-beam velocity component of precipitation particles within that beam. To retrieve all three components of the wind field, two (or more) Doppler radar beams must scan an area with a sufficient separation angle between the beams (e.g., Armijo 1969; Klimowski and Marwitz 1992). Airborne radars must therefore employ certain scanning techniques

Corresponding author address: Anthony C. Didlake Jr., NASA/GSFC, Mail Code 612, Greenbelt, MD 20771.
E-mail: anthony.didlake@nasa.gov

DOI: 10.1175/JAMC-D-14-0203.1

© 2015 American Meteorological Society

that provide multiple views of the wind from sufficiently different angles in order to map the wind structure of the precipitation phenomena.

In one of the first airborne Doppler studies, Marks and Houze (1984) utilized a scanning technique for successful mapping of the three-dimensional wind field. They used data collected by the X-band Doppler radar on board the National Oceanic and Atmospheric Administration (NOAA) WP-3D (P3) aircraft. Located in the tail of the aircraft, the radar antenna pointed orthogonally to the aircraft track and scanned circularly through all elevation angles around a horizontal axis [for more on this radar, see Jorgensen (1984)]. Multiple viewing angles of the same domain were obtained by flying the aircraft at different track angles. Another tail radar was later installed on the second NOAA P3 aircraft, allowing for simultaneous Doppler observations when both aircraft were flown together (Gamache at al. 1995). Both tail radars soon implemented the fore/aft scanning technique (FAST; Jorgensen and DuGranrut 1991), in which the antenna alternately points ~20° to the fore and aft of the aircraft while circularly sweeping around a horizontal axis. With this technique, multiple along-beam velocity measurements from the same domain are obtained along a single flight track by the different fore and aft angles. The National Center for Atmospheric Research Electra Doppler Radar (ELDORA) operates with the same scanning geometry but utilizes two antennas that rotate at a faster rate, allowing for higher-resolution observations (Hildebrand et al. 1996).

Multiple techniques for retrieving the three-dimensional wind field have been developed for the NOAA P3 tail radar and the ELDORA, which both scan around a horizontal axis. One such method is a local solver that interpolates radial velocities from each viewing angle onto a Cartesian grid and solves for the corresponding velocities in the horizontal plane. These horizontal velocities from different viewing angles are then used to calculate two orthogonal horizontal wind components (e.g., Jorgensen et al. 1983; Marks and Houze 1984). The vertical wind component is calculated by integrating the anelastic mass continuity equation using appropriate boundary conditions. This technique is simple and computationally inexpensive, but errors can accumulate in the wind component along the direction of integration (Gao et al. 1999).

A second method is a global optimization approach that minimizes a cost function containing the differences between the radar-measured and retrieved velocity components. This cost function also includes constraints such as the anelastic mass continuity equation and vertical velocity boundary conditions (Gamache 1997; Bousquet and Chong 1998; Reasor et al. 2009). With the avoidance of explicit integration, this variational technique reduces errors in the vertical velocity for the aforementioned scanning geometry (Gao et al. 1999). Since all retrieval strategies are limited by the geometry of the scanning technique, no individual retrieval method is perfect; however, utilizing multiple methods adds to the reliability of the scientific interpretations of the retrieved wind fields.

The High-Altitude Imaging Wind and Rain Airborne Profiler (HIWRAP), recently developed at NASA's Goddard Space Flight Center, is a Doppler radar system that employs a different scanning strategy from the previously mentioned airborne Doppler radars (Li et al. 2011). It operates with two beams that point downward at fixed angles (30° and 40° away from nadir) with each beam scanning conically around a vertical axis. HIWRAP flew for the first time in 2010 on the NASA Global Hawk unmanned aircraft during the Genesis and Rapid Intensification Processes (GRIP) field experiment (Braun et al. 2013).

Recent studies have begun exploring how established retrieval methods can be applied to the scanning geometry of HIWRAP. Tian et al. [2013; here and below see also Tian (2014, manuscript submitted to *J. Appl. Meteor. Climatol.*)] applied the velocity azimuth display (VAD) technique (Lhermitte and Atlas 1961; Browning and Wexler 1968) to HIWRAP data to obtain the mean vertical profile of the horizontal wind along the flight track. Under the assumptions that the wind field is linear and the vertical velocity is constant across the scan circle, this method fits the measured radial winds at each altitude to a sinusoidal curve as a function of azimuth. Guimond et al. (2014) implemented the global optimization technique to obtain the three-dimensional wind field in the HIWRAP scanning domain. The cost function for this variational scheme included a modified weighting parameter that was better suited for the different scanning geometry.

In this paper, we extend the application of established retrieval techniques to the HIWRAP geometry by focusing on a simple interpolation and integration approach. The vertical integration scheme used for the P3 tail radars cannot be applied in the HIWRAP case since the scanning geometry does not align sufficiently with the horizontal wind in order to avoid large projection errors introduced by the vertical wind. A better alternative is the coplane method described by Armijo (1969) and Miller and Strauch (1974). The coplane method uses a cylindrical coordinate system in which two components of the wind are readily derived from the observations. The third wind component is completely unobserved by the radar and must be retrieved by explicitly integrating the mass continuity equation with specified boundary conditions. As a local solver, the solution of the coplane method at

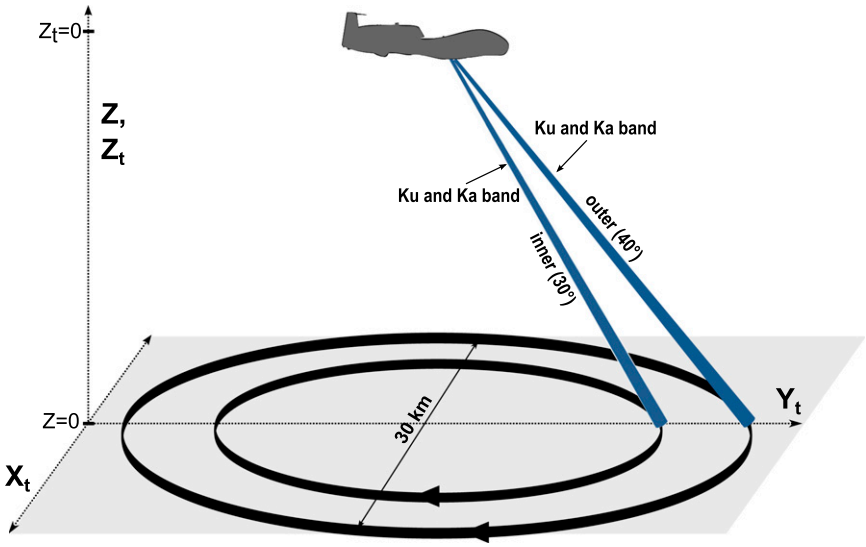

FIG. 1. Schematic showing the scanning technique of the HIWRAP radar in a track-following Cartesian coordinate framework (X_t, Y_t, Z_t). Two beams, each with Ku and Ka bands, point downward at two angles and scan conically around a vertical axis. For a stationary radar and plane at its typical altitude of 18.5 km, the outermost beam scans a circle at the surface ($Z = 0$) with an approximate diameter of 30 km.

a certain grid point has a transparent relationship to the local radar observations, whereas in a global solver observations across the radar domain have an impact on the solution at an individual grid point. Without such interference, possible errors in the radar measurements or retrieved winds are more easily identifiable and traceable. With a natural coordinate system, the coplane method is particularly useful for understanding the advantages and disadvantages of the HIWRAP scanning technique. This understanding is necessary for interpreting any Doppler analysis method used on the HIWRAP radar geometry. In this study, we apply the coplane technique to simulated radar data and actual radar data to demonstrate its effectiveness. We also compare this technique to the global optimization solutions and investigate their differences.

Sections 2 and 3 describe the coplane method and its application to the HIWRAP geometry and observations. Section 4 examines the boundary conditions necessary for the coplane method. Section 5 analyzes the coplane retrieval of simulated radar data and section 6 analyzes the coplane retrieval of real HIWRAP data. Section 7 presents the conclusions of this study.

2. Coplane method and HIWRAP geometry

a. Description of HIWRAP

HIWRAP is a dual-beam, dual-frequency (Ka and Ku band) radar system designed to fly on the high-altitude NASA Global Hawk unmanned aircraft system. Rather than scanning around a horizontal axis like the tail radars on the P3 aircraft, the antenna beams of HIWRAP point downward and scan around a vertical axis to obtain multiple angled looks of the tropospheric winds. Figure 1 illustrates this scanning geometry. The two beams point at nominal tilt angles τ of 30° and 40° away from nadir, while the antenna rotates at a typical rate of $100° \, s^{-1}$, such that one complete revolution takes about 3.5 s. The radar beams, each with a range resolution of 150 m, sweep out spiral paths over the ground as the aircraft flies with an ideal level position along a straight flight track. For a typical aircraft speed of $160 \, m \, s^{-1}$ and altitude of 18.5 km, the along-track sampling and swath width are 560 m and ~30 km, respectively. The outer beam operates simultaneously at 13.5 and 33.7 GHz and the inner beam operates simultaneously at 13.9 and 35.6 GHz. HIWRAP employs dual-pulse repetition frequency sampling that can yield an extended unambiguous velocity of $\sim 110 \, m \, s^{-1}$. A more detailed description of HIWRAP can be found in Li et al. (2011).

b. Description of the coplane method

The coplane dual-Doppler technique was developed to retrieve the three-dimensional winds with two or more ground radars (Armijo 1969; Miller and Strauch 1974) and later applied to airborne tail radars employing the FAST (Chong and Testud 1996). This technique is implemented in a cylindrical coordinate system whose central axis is the line between the location points where

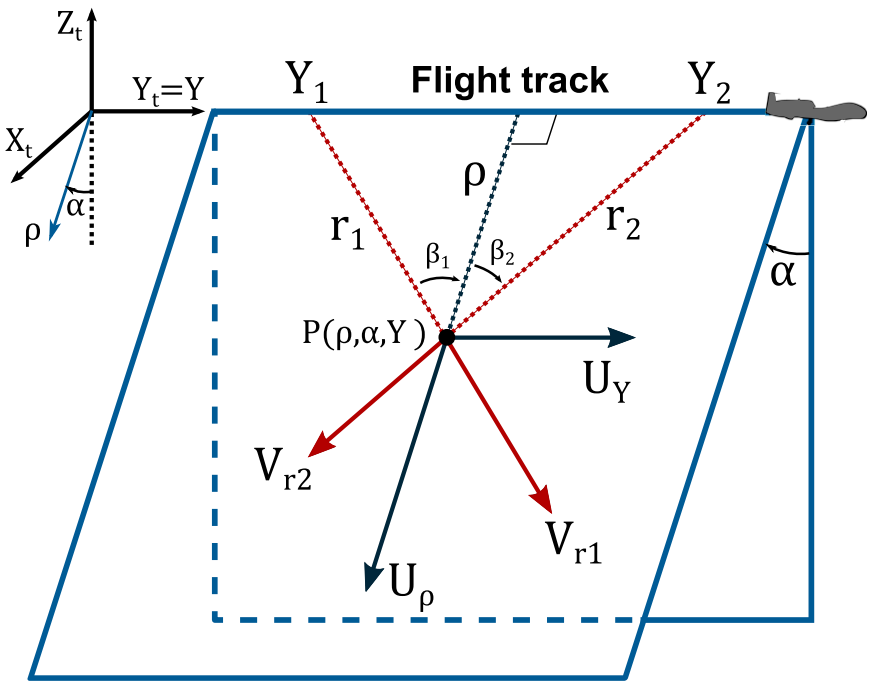

FIG. 2. Cylindrical coordinate system used for the coplane dual-Doppler retrieval from HIWRAP observations. The position of the target in the cylindrical coordinate system is P, defined by the radius ρ, coplane angle α, and flight track distance Y. The red dashed lines and red arrows represent line segments and vectors, respectively, along the radar beam. The black dashed line and black arrows within the coplane represent a line segment and vectors in the cylindrical coordinate system. The symbols r_1 and r_2 are the ranges of the target from the radar positions at Y_1 and Y_2. Angles β_1 and β_2 are the positive angles between the ranges and the radius ρ. Components V_{r1} and V_{r2} are the radial Doppler velocities at point P, and U_ρ and U_Y are the corresponding cylindrical coordinate velocity components in the coplane. The axes X_t, Y, and Z_t define the corresponding track-following Cartesian coordinate framework, where Y_t is coincident with Y. [Figure adapted from Tian et al. (2014, manuscript submitted to *J. Appl. Meteor. Climatol.*).]

the radar (or radars) provides two different looks of a single point in the domain. For aircraft observations, the ideal situation for the coplane method would have a straight flight track and constant flight altitude across the analysis domain. The two looks of the wind field, obtained with fore- and aft-pointing beams, are considered independent and, for the purpose of this study, instantaneous. For the typical Global Hawk speed and altitude, the largest time gap between the observations is 200 s. These two measurements can then be readily converted into two orthogonal wind components. Recovery of the third wind component at every point in the domain requires well-posed data (i.e., data exist at every point). To describe the application of the coplane method to the downward-pointing conically scanning HIWRAP geometry, we follow the discussions from Tian et al. (2014, manuscript submitted to *J. Appl. Meteor. Climatol.*) and Guimond et al. (2014).

Figure 2 illustrates the cylindrical coordinate system defined by ρ, α, and Y. The flight track serves as the main axis Y where the origin is some arbitrary point along Y. The variable ρ is the radial distance from the central axis, and α is the coplane angle beginning at 0° for the nadir plane and increasing to the right of the flight track. For every rotation angle θ (0° points in $+Y$ direction), range r, and current track position Y_1, observations are first mapped onto a track-following Cartesian grid by

$$\begin{pmatrix} X_t \\ Y_t \\ Z_t \end{pmatrix} = r \begin{bmatrix} \cos D(a) - \sin D \sin\tau(b) - \sin D(c) \\ Y_1/r + \sin D(a) + \cos D \sin\tau(b) + \cos D(c) \\ \sin\tau(\sin P \cos\theta - \cos P \sin R \sin\theta) - \cos P \cos R \cos\tau \end{bmatrix}, \tag{1}$$

where

$$\begin{pmatrix} a \\ b \\ c \end{pmatrix} = \begin{pmatrix} \cos R \sin\theta \sin\tau - \sin R \cos\tau \\ \cos P \cos\theta + \sin P \sin R \sin\theta \\ \sin P \cos R \cos\tau \end{pmatrix} \tag{2}$$

and D, P, R, and τ are the drift, pitch, roll, and tilt angles, respectively. Equations (1) and (2) are similar to those in Guimond et al. (2014) and are derived for the current scanning geometry following Lee et al. (1994). The cylindrical coordinates of the observations are then calculated by

$$\begin{pmatrix} \rho \\ \alpha \\ Y \end{pmatrix} = \begin{bmatrix} \sqrt{X_t^2 + Z_t^2} \\ \tan^{-1}\left(\dfrac{X_t}{Z_t}\right) \\ Y_t \end{bmatrix}. \tag{3}$$

As the plane flies along the track, a single beam at a given tilt angle τ obtains Doppler velocities in an α plane when it is located at Y_1 (fore) and Y_2 (aft). These velocities are interpolated onto the cylindrical coordinate grid so that each grid point P contains consolidated fore and aft radial velocities (V_{r1} and V_{r2}, respectively), as seen in Fig. 2. Orthogonal velocities in the α plane are then calculated by

$$U_\rho = \frac{-r_1(Y - Y_2)V_{r1} + r_2(Y - Y_1)V_{r2}}{\rho(Y_2 - Y_1)} \quad \text{and}$$
$$U_Y = \frac{r_1 V_{r1} - r_2 V_{r2}}{Y_2 - Y_1}, \tag{4}$$

where $r_1 = \sqrt{\rho^2 + (Y - Y_1)^2}$ and $r_2 = \sqrt{\rho^2 + (Y - Y_2)^2}$. From these standard dual-Doppler calculations, we obtain two velocity components (U_ρ, U_Y) in each α plane on the cylindrical grid.

The separation angle β, defined as $\beta = \beta_1 + \beta_2$ as seen in Fig. 2, is the angle between the fore and the aft beams. The angles β_1 and β_2 are calculated by

$$\beta_n = \sin^{-1}(|Y - Y_n|/r_n), \tag{5}$$

where β_n represents either β_1 or β_2. Combining Eqs. (1)–(3) and assuming all attitude angles are equal to 0, Eq. (5) can be rewritten as

$$\beta_n = \sin^{-1}\{\cos\tau_e \cos[\sin^{-1}(\tan\tau_e \tan\alpha)]\}, \tag{6}$$

where β_n is now a function of the coplane angle α. Equation (6) uses the elevation angle τ_e, which is defined as $\tau_e = \tau - 90°$. The separation angle directly corresponds to the accuracies of the two retrieved wind components, U_ρ and U_Y. In applying the error estimates of Doviak et al. (1976) and trigonometric substitutions to Eq. (4), the variances of the two wind components are specified by

$$\sigma_\rho^2 = \frac{\sigma_{r1}^2 + \sigma_{r2}^2}{4\cos^2\beta_1} \quad \text{and} \quad \sigma_Y^2 = \frac{\sigma_{r1}^2 + \sigma_{r2}^2}{4\sin^2\beta_1}, \tag{7}$$

where σ_{r1} and σ_{r2} are the errors of V_{r1} and V_{r2}. The errors σ_{r1} and σ_{r2} are equal to each other given that V_{r1} and V_{r1} are independent measurements. Tian et al. (2014, manuscript submitted to *J. Appl. Meteor. Climatol.*) determined that the standard error of HIWRAP Doppler estimates for the Ka band is $\sigma_r = 0.46\,\mathrm{m\,s^{-1}}$. Equation (7) assumes that all errors are Gaussian distributed. Other sources of error can contribute to σ_r such as velocity unfolding error and error due to aircraft motion. For the analysis in section 6, we verified that the Doppler velocities were unfolded properly. The Doppler velocities were also corrected for aircraft motion using attitude information (i.e., roll, drift, and pitch).

Figure 3 shows the separation angle and the corresponding wind variances as a function of the coplane angle for the two tilt angles of the HIWRAP geometry. It is shown that β reaches its peak at nadir and then decreases as α increases in magnitude. We find that σ_Y^2 is lowest at nadir and remains below $0.6\,\mathrm{m^2\,s^{-2}}$ throughout most of the domain. Toward the domain edges, the fore and aft beams become closely parallel (i.e., β approaches 0°) and point less in the along-track direction. Consequently, the accuracy of the retrieved U_Y quickly degrades at large α magnitudes. On the other hand, the U_ρ component is accurately estimated ($\sigma_\rho^2 < 0.2\,\mathrm{m^2\,s^{-2}}$). It is most accurate near the domain edges and least accurate at nadir. Still, the magnitudes of σ_ρ^2 and the corresponding changes with α are lower than those of σ_Y^2. Studies have shown that the two in-plane wind components can both be retrieved with reasonable accuracy when the separation angle is at least 30° (e.g., Klimowski and Marwitz 1992). In this scanning geometry, the outer beam retrieves the wind components with reasonable accuracy when $|\alpha| < 37.5°$, where $\sigma^2 < 1.56\,\mathrm{m\,s^{-1}}$ for both components.

Figure 3 also shows that the outer beam retrieves U_Y more accurately while the inner beam retrieves U_ρ more accurately within its smaller domain. We incorporate observations from both beams by weighting these relative retrieval accuracies. For each grid point within the domain of the inner beam, the composite wind components are

$$U_\rho = \frac{\sigma_{\rho i}^2 U_{\rho o} + \sigma_{\rho o}^2 U_{\rho i}}{\sigma_{\rho i}^2 + \sigma_{\rho o}^2} \quad \text{and}$$
$$U_Y = \frac{\sigma_{Yi}^2 U_{Yo} + \sigma_{Yo}^2 U_{Yi}}{\sigma_{Yi}^2 + \sigma_{Yo}^2}, \tag{8}$$

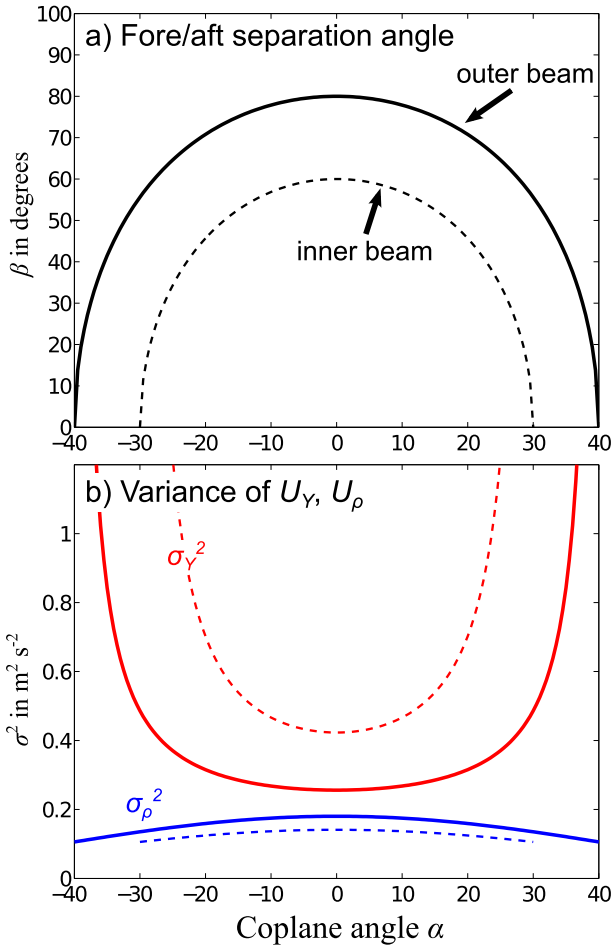

FIG. 3. (a) The separation angle β as a function of the coplane angle α for the inner beam (dashed black) and the outer beam (solid black). (b) Variance (σ^2) of the U_Y (red) and U_ρ (blue) wind components due to Doppler estimate error as a function of the coplane angle α. Variances are calculated for the Ka-band inner (red dashed and blue dashed) and outer (red solid and blue solid) beams.

where the i and o subscripts denote observations from the inner and outer beams.

The third component of the wind, U_α, is retrieved by integrating the anelastic mass continuity equation along the α axis away from the nadir plane. Figure 4 illustrates the two integration directions that span the radar domain. The anelastic mass continuity equation is given by

$$\frac{\partial(\rho\eta U_r)}{\partial\rho} + \frac{\partial(\eta U_\alpha)}{\partial\alpha} + r\frac{\partial(\eta U_Y)}{\partial Y} = 0, \tag{9}$$

where η is the air density. The current calculations use the Jordan (1958) standard tropical Atlantic Ocean air density profile. Using the square rule for integration on Eq. (9), U_α is obtained by

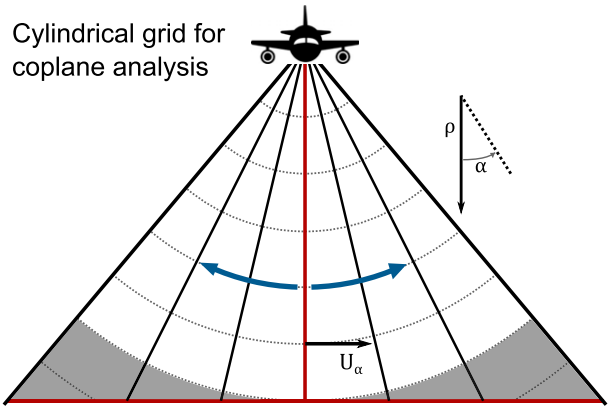

FIG. 4. Diagram of the cylindrical grid (ρ, α) along a given Y location. Red lines indicate the boundary condition locations for initialization of the U_α wind component. Blue arrows indicate the integration directions for retrieving the U_α wind component. The shaded region shows the area initialized by the surface boundary condition.

$$\eta U_\alpha\Big|_{\alpha_1} = \eta U_\alpha\Big|_{\alpha_0} - \frac{1}{2}(\alpha_1 - \alpha_0)[f(\alpha_1) + f(\alpha_0)] \quad \text{and}$$
$$f(\alpha) = \frac{\partial(\rho\eta U_r)}{\partial\rho} + r\frac{\partial(\eta U_Y)}{\partial Y}, \tag{10}$$

where the subscripts 0 and 1 denote the previous and current integration locations. As depicted in Fig. 4, U_α must be initialized with boundary conditions at the nadir plane and at the surface. To retrieve U_α at all points, the data must exist at all points in the domain. If radial velocities are missing at any point, U_α cannot be calculated at points along the integration path beyond the missing point. Data may continue beyond the missing point allowing for calculation of U_Y and U_ρ.

The nadir boundary condition is obtained by taking observations at small angles away from nadir on either side. In the track-following Cartesian grid, the Cartesian coordinate cross-track (u), along-track (v), and vertical (w) velocities are related to the cylindrical coordinate velocities by

$$U_\rho = u\sin\alpha - w\cos\alpha, \tag{11}$$

$$U_Y = v, \quad \text{and} \tag{12}$$

$$U_\alpha = u\cos\alpha + w\sin\alpha. \tag{13}$$

Suppose that U_ρ components ($U_{\rho1}$, $U_{\rho2}$) are calculated at a small angle α on either side of nadir ($\alpha_1 = +\alpha$; $\alpha_2 = -\alpha$) at a constant radius. For the two U_ρ components, we make the assumption that w is constant and u is linear across the span of the U_ρ locations. It follows from Eq. (11) that u at nadir (u_0) is expressed by

$$u_0 = \frac{U_{\rho 1} - U_{\rho 2}}{2\sin\alpha} \tag{14}$$

for each altitude corresponding to the radius of the U_ρ observations. Since $U_\alpha = u_0$ at nadir, Eq. (14) gives the boundary conditions for initializing U_α along the nadir plane. To calculate the nadir boundary condition, we chose a value of $\alpha = 3.35°$ for the outer beam and $\alpha = 2.31°$ for the inner beam. The two u_0 values from each beam at each point are combined according to the U_ρ calculation and error estimates from Eq. (8). This weighting was selected since the final values rely on U_ρ calculations.

At the surface, the impermeability condition ($w = 0$) is applied as a boundary condition. By setting w equal to 0, Eqs. (11) and (13) lead to

$$U_\alpha\Big|_{z=0} = \frac{U_\rho}{\tan\alpha}. \tag{15}$$

With this relationship, U_ρ can be used to initialize U_α at the surface. The surface boundary condition works well in an idealized setting where accurate observations are available near the surface and the surface is flat. However, in actual aircraft observations over water, sea spray can contaminate the Doppler measurements and the surface is not flat. We address these surface issues and assess the nadir boundary condition in section 4.

3. Data and methods

a. Radar simulator

To assess the validity of the coplane analysis, we use model output and a radar simulator designed after Guimond et al. (2014) with no added noise or aircraft attitude. The radar simulator mimics the scanning technique of the HIWRAP radar and obtains radial velocities V_r from the modeled velocity fields as the radar moves along a straight, level track. The model used is the nonhydrostatic fifth-generation Pennsylvania State University–National Center for Atmospheric Research Mesoscale Model (MM5). We take an MM5 simulation of Hurricane Rita (2005) at a single time frame near its peak intensity (maximum wind speed of 75 m s^{-1}). The model output has a horizontal resolution of 1.67 km and 28 sigma levels in the vertical. Two simulated radar beams are positioned at 30° and 40° tilt angles, and rotate at a period of 3.5 s per revolution with an azimuthal resolution of 2° and a range resolution of 150 m. The radar has a nominal altitude of 18.5 km and the simulated aircraft has a ground speed of 160 m s^{-1}. Shown in Fig. 5, the track has a length of 200 km and passes through the center of the storm.

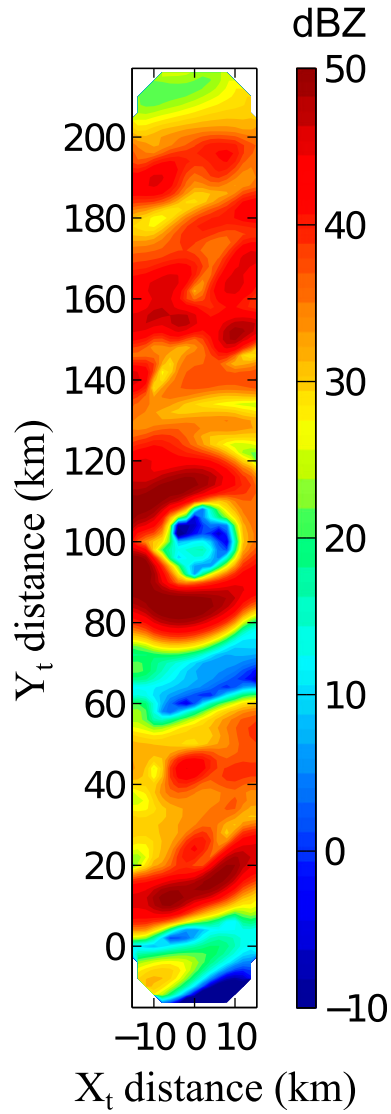

FIG. 5. Plan view of model reflectivity at 2-km altitude. The data are HIWRAP radar simulator observations of a model simulation of Hurricane Rita at peak strength.

b. Real data

On 15 September 2013, the NASA Global Hawk AV-1 flew over Hurricane Ingrid as part of the NASA Hurricane and Severe Storm Sentinel (HS3) field campaign. The HIWRAP radar on board the Global Hawk observed the northern edge of Ingrid as the storm tracked west across the Gulf of Mexico. The data used in this study were taken from 1836 to 1900 UTC. Figure 6 shows the HIWRAP observed reflectivity (plan view and at nadir) along with the corresponding infrared satellite image. In section 6, we apply the coplane analysis to the Ka-band outer beam observations. To remove noise, pixels with reflectivity less than 0 dBZ

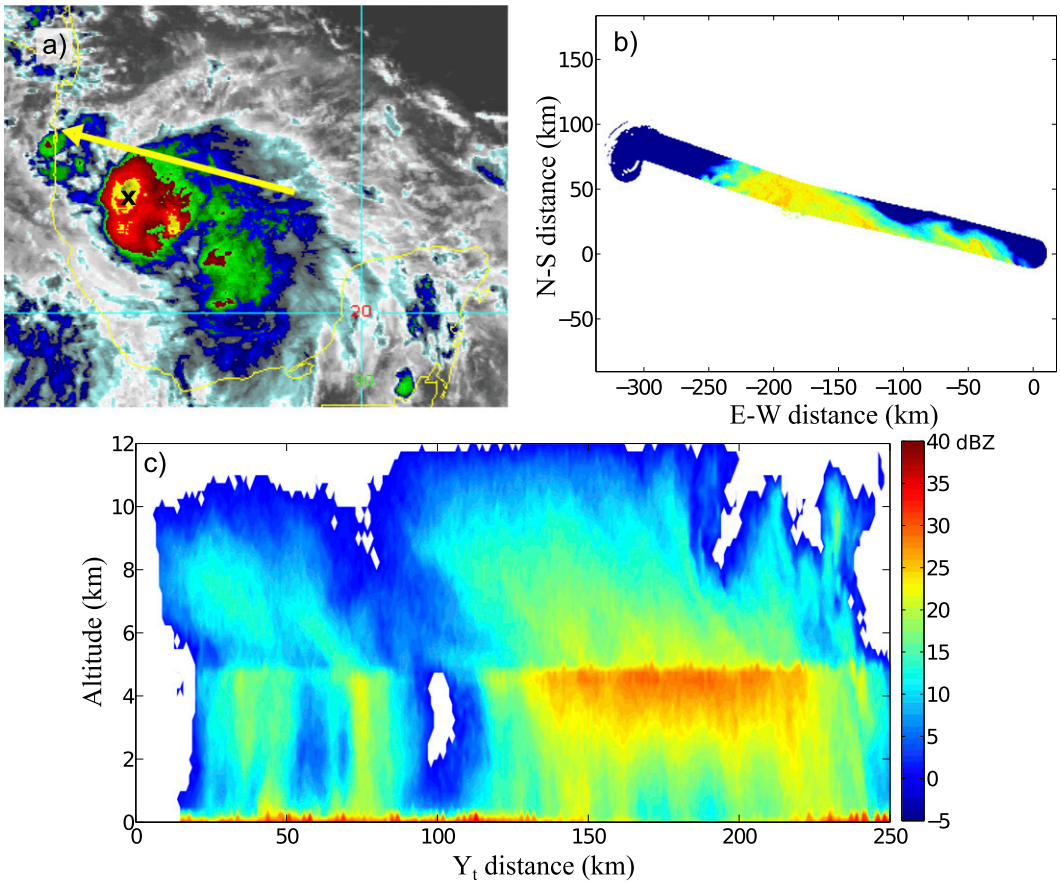

FIG. 6. (a) Infrared satellite imagery of Hurricane Ingrid (2013) with the flight track from 15 Sep 2013 of the NASA Global Hawk AV-1 overlain in yellow. A black × marks the best-track storm center. (b) The 1.5-km Ka-band outer beam reflectivity observed by HIWRAP along the flight track from (a). Observations were taken from 1836 to 1900 UTC. (c) Nadir view of Ka-band outer beam reflectivity. The graph origin is the eastern end of the plan-view reflectivity from (b).

were not used in the analysis. The Doppler velocities were unfolded according to Dazhang et al. (1984). We applied corrections for beam-pointing errors by aligning the expected range of the ocean surface with the range of the observed surface return. Fall speed corrections from Heymsfield et al. (2010) were also applied to the velocity data. In this correction algorithm, fall speeds were calculated as a function of the Ka-band reflectivity and altitude.

c. *Grid and interpolation specifications*

The coplane method requires an initial interpolation of radial velocity data onto a cylindrical grid. The cylindrical grid used in this study has a radial resolution of 0.5 km, along-track resolution of 2 km, and azimuthal resolution of 2.5°. The observations (both simulated and real) are interpolated onto this grid using a Barnes weighting scheme (Barnes 1973; Koch et al. 1983), given by

$$w_m = \exp\left[-\left(\frac{r_m}{\gamma\delta}\right)^2\right], \tag{16}$$

where r_m is the distance of the mth observation from the analysis grid point, γ is a chosen shape parameter, and δ is the influence radii expressed by

$$\delta = \sqrt{r_\rho^2 + r_Y^2 + r_\alpha^2}, \tag{17}$$

where r_ρ, r_Y, and r_α are the radii of influence in the three coordinate directions. For this interpolation, the radial, horizontal, and azimuthal radii of influence are 0.5 km, 2 km, and 1.25°, respectively. The 1.25° azimuthal radius of influence has an equivalent distance of 2 km and the shape parameter γ, which determines the width of the weighting function, is chosen as 0.75. Following the coplane calculations, the data are converted into Cartesian coordinate velocities via Eqs. (11)–(13) and are finally

interpolated into Cartesian coordinates. The Cartesian grid has a horizontal resolution of 2 km and a vertical resolution of 1 km. An additional level is added at 0.5-km altitude to better resolve the low-level winds. This interpolation uses the same Barnes filter but with a radius of influence of 2 km in the horizontal dimensions and 0.25 km in the vertical dimension. By determining the response function of the Barnes filter (Koch et al. 1983), the minimum resolvable horizontal wavelength is calculated to be 4 km, which is also twice the horizontal grid spacing.

4. Boundary conditions analysis

a. Nadir boundary conditions analysis

At nadir, the cross-track wind component is unobserved by the HIWRAP radar and must be estimated by utilizing other available measurements. It is important to obtain a good estimate of the cross-track wind at nadir as this will serve as the boundary condition that initializes the U_α wind component for integration throughout most of the domain. As shown in Eq. (14), we estimate the cross-track wind by using wind measurements taken at a small angle α away from nadir. Choosing a value for α requires a balance of certain trade-offs. For smaller α values, the distance between observations is smaller and thus the assumptions of constant vertical velocity and linear cross-track velocity are well suited. However, at angles that are closer to zero, the wind measurements are more susceptible to errors in the cross-track velocity. For larger α values, the cross-track wind is better sampled and this reduces the susceptibility to measurement errors; however, the distance between observations is greater, making the necessary assumptions less suitable.

We use the simulated radar data to choose a value for α. Boundary condition estimates are calculated with varying α values, which are then compared to the model "truth" cross-track velocities. This calculation requires interpolation of radial velocities to the different α planes. A Barnes filter is used for the interpolation with the influence radii specified in section 3c. Assuming all attitude angles are equal to zero, Eqs. (1)–(3) yield α as a function of the rotation angle θ and the elevation angle τ_e:

$$\alpha = \tan^{-1}\left(\frac{\sin\theta\cos\tau_e}{\sin\tau_e}\right). \tag{18}$$

The α values are tested by varying the deviation of θ from the nadir plane. For example, the rotation angles 2° and 178° lie along the plane $\alpha = 1.677°$ for the outer beam. Correspondingly, the rotation angles 358° and 182° lie along the plane $\alpha = -1.677°$. Figure 7a shows the coplane angles for the varying rotation angle, while Fig. 7b presents

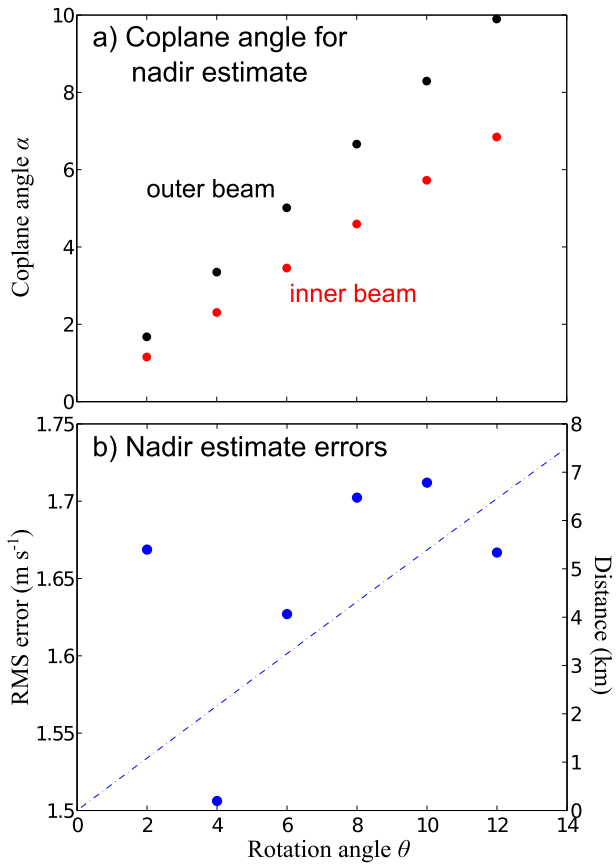

FIG. 7. (a) The coplane angle α as a function of rotation angle calculated from Eq. (18). Results from the inner beam (red) and outer beam (black) are shown. (b) RMS errors of U_α in the nadir boundary conditions estimate for varying rotation angles (dots) and cross-track distance between outer-beam locations for varying rotation angles (dashed line).

the root-mean-square (RMS) errors for the different estimates. The errors are all relatively small in comparison with the wind speeds of the simulated hurricane. For a wind speed of 30 m s^{-1}, the largest error in Fig. 7b constitutes 5% of this wind speed. The α values corresponding to $\theta = 4°$ produced the smallest error, so we chose these values for the boundary condition retrieval. As seen in Fig. 7b, the angle $\theta = 4°$ corresponds to a cross-track distance between observations of 2.2 km at the surface.

Figure 8 displays the estimated U_α at nadir along with the errors relative to the model truth. The retrieved wind field captures the overall structure of the hurricane. Errors larger than 2 m s^{-1} occur near the eyewall region ($Y = 85$ and 115 km), the surface, and the domain edge at $Y = 18$ km. These positive errors at the domain edge reach 8 m s^{-1}. The largest negative errors occur in the midlevels near $Y = 155$ km, reaching values of -9 m s^{-1}. These errors stem from local violations of the assumptions made in the calculation of Eq. (14). Specifically,

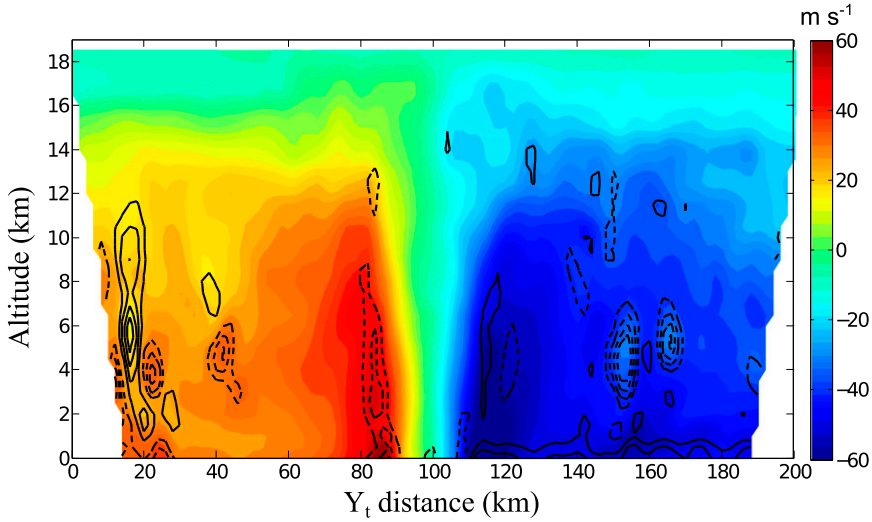

FIG. 8. The U_α wind component at nadir retrieved from the radar simulator data using the coplane analysis. Deviations from the model truth are shown in black contours at intervals of $2\,\mathrm{m\,s^{-1}}$. Dashed lines are negative values beginning at $-2\,\mathrm{m\,s^{-1}}$, and solid lines are positive values beginning at $2\,\mathrm{m\,s^{-1}}$. See text for details.

violations of the constant vertical velocity assumption are the primary source of error in Fig. 8, where vertical velocity deviations of $0.5\,\mathrm{m\,s^{-1}}$ produced U_α errors of $\sim 3\,\mathrm{m\,s^{-1}}$.

b. Surface boundary condition analysis

The values of U_α must be initialized at the lower boundary of the analysis domain. Given the curved paths of integration, this initialization affects the lower portion of the domain that increases in depth away from nadir (as indicated in Fig. 4). As described in section 2, the lower boundary initialization can be done most simply by invoking the impermeability condition and setting $w = 0$ at the surface [Eq. (15)]. This condition requires reliable observations near a flat surface, which is an ideal situation that models provide. The initialization locations on the surface are not necessarily points on the cylindrical grid, but U_α can still be effectively initialized for every integration path that intersects the surface.

With actual observations, setting the surface boundary condition cannot be done so simply, particularly over the ocean surface as in the case of tropical cyclone research. The ocean surface may not be flat and sea spray can contaminate echoes near the surface. Previous dual-Doppler methods approach the surface initialization of the integrated wind component (usually w) differently. In the Cartesian Editing and Display of Radar Data under Interactive Control software (CEDRIC; Mohr et al. 1986), the vertical velocity can be initialized at the lowest level of usable data by setting w equal to a specified multiple of the locally measured horizontal divergence. Chong and Testud (1996) use a variational method in which w at all surface locations vary near $w = 0$ such that the resulting U_α field contains a minimum amount of continuity irregularities.

For this study, we use a simple approach that initializes U_α at the lowest cylindrical grid points closest to a selected low-level altitude. In the simulated data, we choose 0.5 km as the lowest level of available data, which is approximately the lowest level of usable data from the HIWRAP observations. For this cylindrical coordinate system, the lower boundary grid points are not all at the same altitude. By combining Eqs. (11) and (13), U_α at each lower boundary point is given by

$$U_\alpha = \frac{U_\rho}{\tan\alpha} + w\left(\frac{\cos^2\alpha}{\sin\alpha} + \sin\alpha\right). \tag{19}$$

Using this equation, U_α is initialized with the local U_ρ. Additionally, we estimate w from the vertical velocity calculated at nadir (where $w = -U_\rho$) for that corresponding altitude and Y location.

The calculated lower-bound U_α values were compared with the model truth and resulted in an RMS error of $2.05\,\mathrm{m\,s^{-1}}$. Moreover, the lower-bound U_α values stemming from the original impermeability condition resulted in an RMS error of $1.69\,\mathrm{m\,s^{-1}}$. As expected, the accuracy of the nadir-w approach is slightly lower than that of the impermeability approach; however, the difference in the errors ($0.36\,\mathrm{m\,s^{-1}}$) is small relative to the near-surface hurricane wind speeds (which have magnitudes greater than $30\,\mathrm{m\,s^{-1}}$ outside the eye). From this analysis, the nadir-w approach represented by Eq. (19) is deemed suitable for U_α initialization for near-surface grid points.

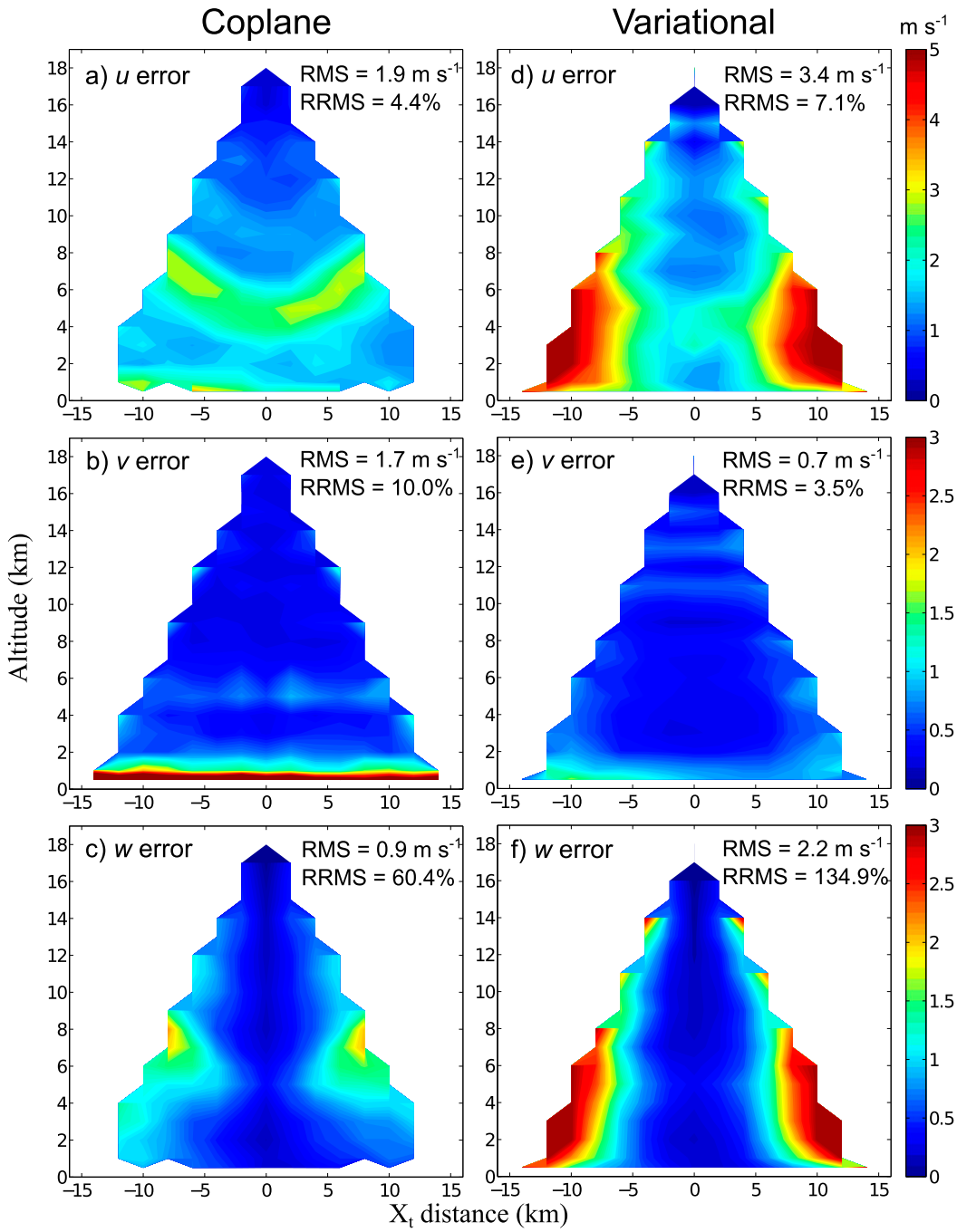

FIG. 9. RMS errors of the two retrieval methods. Errors from the coplane analysis are shown for the (a) cross-track (u), (b) along-track (v), and (c) vertical (w) wind components. (d)–(f) Errors from the variational analysis for the same wind components. Error fields are averaged along the flight track. Overall RMS and relative-RMS errors are also given (m s^{-1} and %, respectively).

5. Retrieval error analysis

In this section, we use the simulated radar data to examine the wind field retrieved from the coplane analysis. As described in the previous section, we do not use radar radial velocities below 0.5-km altitude in this retrieval. Figures 9a–c present the RMS errors calculated along the flight track for the retrieved cross-track (u), along-track (v), and vertical velocity (w) components. These figures show the total errors and the error patterns of each wind component for the HIWRAP scanning geometry. The total relative-RMS (RRMS)

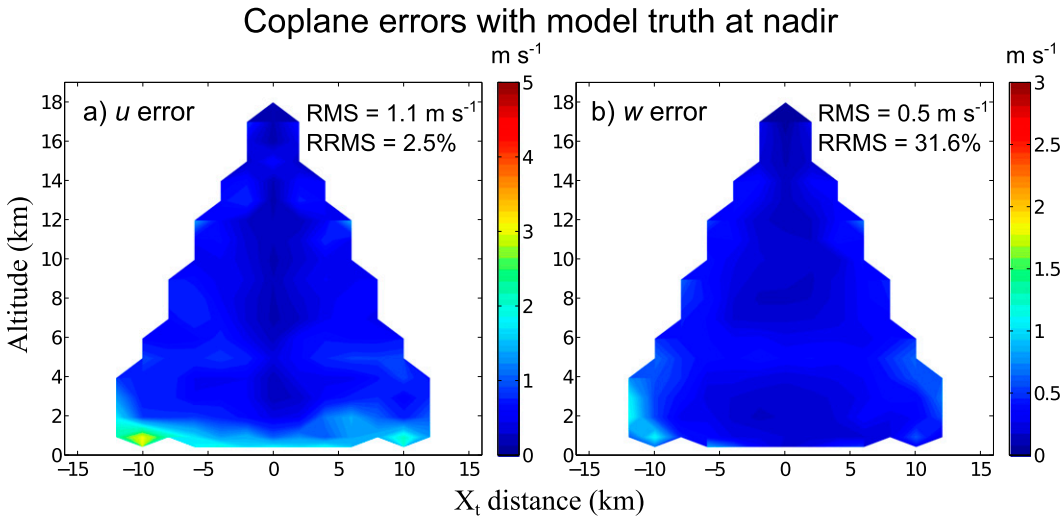

FIG. 10. RMS errors of the coplane analysis for the (a) cross-track (u) and (b) vertical (w) wind components averaged along the flight track. This analysis uses nadir and lower-bound boundary conditions given by the model truth field. Overall RMS and relative-RMS errors are also given (m s^{-1} and %, respectively).

error in each figure is a normalization of the errors relative to the velocity magnitudes.

The cross-track component u contains an average error of 1.9 m s^{-1}, which, as indicated by the relative-RMS value of 4.4%, is a low value relative to the u magnitudes. Calculation of u depends on both the U_α and U_ρ components, but the u errors largely stem from errors in U_α, as this component is larger and more aligned with u throughout the domain. The u errors form a curved pattern as they follow the integration path upon which U_α was calculated. The largest errors occur near the surface and in a midlevel belt positioned between 4- and 6-km altitude at nadir.

The vertical velocity w contains an average error of 0.9 m s^{-1}, which is significant relative to the vertical velocity magnitudes (RRMS = 60.4%). Despite this significant average error, the error distribution in Fig. 9c shows that the vertical velocities near nadir have the smallest errors and therefore are the most useful. The errors increase as the α angle magnitude increases toward the edges of the domain, with particularly large magnitudes at locations that coincide with the u error belt in Fig. 9a. At these larger α angles, U_α makes an increasing contribution to determining w. As a result, U_α errors that are small relative to the horizontal winds can lead to significant w errors near the domain edges.

We have explained that errors in the u and w fields are mostly due to U_α errors. These errors in the U_α component accumulate during the integration of the wind field for two reasons. First, the divergence of the wind field in the α planes is not well sampled, particularly near the domain edges where U_Y calculations become less accurate (Fig. 3b). Second, U_α is incorrectly initialized for the two boundary conditions. We briefly test which reason is most responsible for the U_α errors by substituting the lower-bound and nadir U_α estimates with the model truth. Figure 10 shows the RMS error patterns. Having the best initialization possible, the wind field errors are significantly reduced to 1.1 m s^{-1} for u and 0.5 m s^{-1} for w. The u error no longer contains the belted pattern and the corresponding w errors along the domain edges are removed. This analysis suggests that the errors in the u and w wind fields are mostly a result of errors in the boundary conditions. The remaining errors are less pronounced in Fig. 10 and can be attributed to divergence sampling and interpolation error.

The along-track component v is the only Cartesian coordinate component that is not calculated with the U_α component. The v errors are very small throughout most of the domain. The largest errors, reaching up to 5 m s^{-1}, occur at 0.5-km altitude. These errors at the lowest level are largely a result of the interpolation from cylindrical to Cartesian coordinates. The lower-bound points on the cylindrical grid are at different altitudes and are all higher than the 0.5-km level. Since the data below 0.5 km were not used, these lower-bound points are the only source of information for interpolation onto the 0.5-km level, which contributes to errors found at this lowest level for all Cartesian wind components. In this particular dataset, the v component (which is largely the radial wind of the hurricane) changes very rapidly at these boundary layer altitudes, resulting in the significant errors found in the lowest levels. When the 0.5-km-level data are excluded from the error analysis, the RMS error drops from 1.7 to 1.0 m s^{-1}.

TABLE 1. Parameters used for the variational dual-Doppler retrieval. Each parameter is explained in detail in Guimond et al. (2014).

Shape parameter (γ)	0.75
Along-track sampling (s)	560 m
Smoothing factor (β)	4
Weighting factor (α_M)	2×2000^2
Weighting factor (α_S)	For simulated data: 0
	For real data: 0.4×2000^4

The coplane analysis is now compared with the global optimization analysis described by Guimond et al. (2014). In their variational method, radar velocities are first interpolated onto a Cartesian grid, and then a modeled wind field is retrieved using the radar velocities, mass continuity, and boundary conditions as constraints. We applied the variational method to the current simulated data using analysis parameters that produced the smallest errors. Specific parameters that were chosen are listed in Table 1.

Figures 9d–f show the RMS errors for the three wind components. The u and w components both have larger overall errors than the coplane analysis. These components, which again are connected to each other through the unobserved wind component U_α, have error patterns that are slightly different from the coplane analysis errors. The best retrievals occur at nadir, and errors increase at all altitudes when approaching the domain edges. These error patterns are consistent with those from Guimond et al. (2014). There is no belt of errors as in Fig. 9a, but increased errors do exist at nadir at the same altitude range of 4–6 km.

Meanwhile, the v field has a smaller overall error than does the coplane analysis. The largest difference in the v error pattern is in the lowest levels. The variational method operates fully in a Cartesian coordinate system, which means that the lowest level of available data coincides with the lowest level of grid points at 0.5-km altitude. As a result, the rapid vertical changes in v are well captured at these levels and there is no interpolation error from changing coordinate systems.

6. Coplane retrieval with real radar data

In the previous section, the coplane retrieval method was successfully applied to simulated radar data. We now apply the coplane method to real HIWRAP data shown in Fig. 6, and we compare the retrieved wind field to a solution from the variational method (Guimond et al. 2014).

Figures 11a–c presents the coplane analysis cross-track (u), along-track (v), and vertical (w) components of the wind field along nadir of the observation domain. The u field contains mostly positive velocities with values $>10\,\mathrm{m\,s^{-1}}$ in the layer below 3 km and the layer above 6 km. In between these layers a midlevel minimum of u occurs. The v field also contains mostly positive velocities that decrease toward the upper levels of the domain (>7-km altitude). When considering the domain location (Fig. 6a), the u and v fields show consistency with the counterclockwise cyclonic circulation of the storm. The cross-track component (Fig. 11a) largely switches from positive to negative values at around $Y_t = 230$ km, which corresponds to the point along the track that is closest to the storm center. Concurrently, the along-track component (Fig. 11b) increases as the track approaches the same closest point.

The reflectivity field shown in Fig. 6c contains a clear brightband signature (at ~4.5-km altitude) and fall streaks, which indicate that the dominant precipitation regime for these observations is stratiform (Houze 1997). In stratiform precipitation, falling ice crystals melt in a layer beneath the 0°C isotherm and form a broad region of light-to-moderate precipitation. The w field (Fig. 11c) shows consistent features with stratiform precipitation, including small magnitudes ($<2\,\mathrm{m\,s^{-1}}$) throughout most of the domain. Updrafts are dominant above the bright band. Below this level, downdrafts are prominent, but a clear exception of positive w values occurs toward the beginning of the domain and at 4-km altitude. These exceptions, which are inconsistent with typical stratiform kinematics, are likely a result of errors in the fall speed correction and/or attenuation of the Ka beam. If these errors were consistent across the radial velocities used in Eqs. (4) and (14) to calculate U_Y and u_0, then the errors would not have an impact on the fields in Figs. 11a,b.

Figures 12a–c present the wind components along a cross section at $Y_t = 160$ km. These cross sections show that the overall patterns seen at nadir extend to the edges of the domain. The midlevel minimum of u grows larger to the right of the flight track (Fig. 12a). Additionally, the downdraft layer (Fig. 12c) also increases in depth to the right of the flight track. The slanted stretches of downdrafts $<-3\,\mathrm{m\,s^{-1}}$ near the domain edges do not appear consistent with expected vertical velocity patterns of stratiform precipitation. Rather, these patterns are reminiscent of the curved error patterns in Figs. 9a,c. Given this resemblance, we infer that these w swaths (and their corresponding u values) contain errors for the same reason as in the radar simulator analysis, which is incorrect initialization of U_α as the boundary condition. By following the curved α paths from these features toward the domain center, one finds that the boundary condition errors occur at nadir between 1- and 2.5-km altitudes in this cross section.

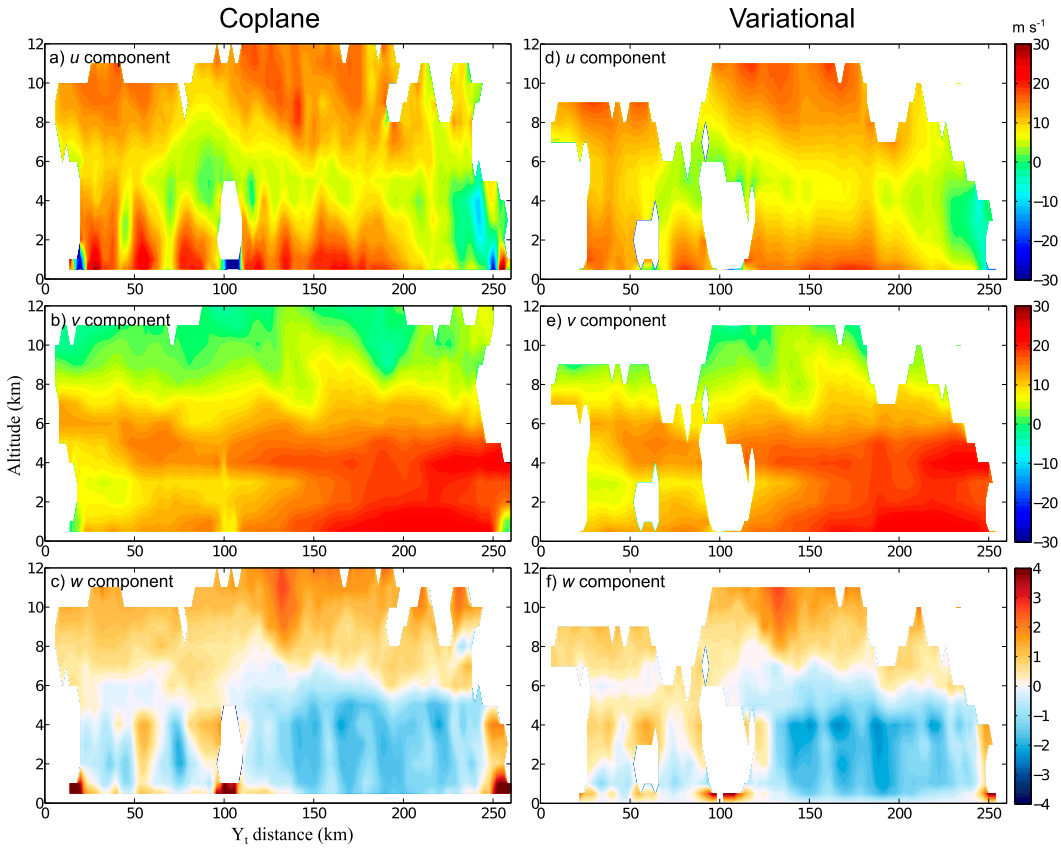

FIG. 11. Nadir view of the (a) u, (b) v, and (c) w wind components as derived by the coplane analysis of the HIWRAP observations seen in Fig. 6. (d)–(f) The variational analysis wind components.

The variational method retrieved a qualitatively similar wind solution as that of the coplane method. Figures 11d–f show that the u and v fields in the nadir plane have the same overall structures as in Figs. 11a–c. Figure 11f mostly has the vertical velocities expected of stratiform precipitation, but this solution takes the same fall speed corrections as in the coplane method and produces noticeably different vertical velocities at the brightband altitude (~4.5 km). The variational u field (Fig. 11d) has noticeably smoother contour patterns than the coplane u field (Fig. 11a), which suggests that the variational method may be filtering out some small-scale features in the data. The v and w fields from both methods do not have a noticeable discrepancy in their contour smoothness. Upon closer inspection, the u field at nadir is impacted most by the smoothing parameter in the variational retrieval. When this smoothing parameter is turned off, the resulting u field appears very similar to the coplane u field.

One advantage of the coplane method is that the minimum resolvable wavelength of the data field is readily determined by calculating the response function of the Barnes filter. On the other hand, determining the minimum resolvable wavelength of the variational method solution is not as straightforward. While a Barnes filter is also used, the weighting parameter is a *constraint* on the optimization and not a direct *calculation*. Thus, the Barnes filter response function cannot exactly determine the minimum resolvable wavelength. In addition, the smoothing parameter certainly increases the minimum resolvable wavelength, but again, this smoothing is a constraint and not a direct calculation. For both the Barnes filter and the Laplacian smoother, the minimum resolvable wavelength must be determined empirically.

Figures 12d–f display the same cross section as in Figs. 12a–c but for the variational solution. As in the coplane analysis, the midlevel u minimum and downdraft layer increase in depth to the right of the flight track. The w field in Fig. 12f does not contain the unrealistic downdraft patterns seen in Fig. 12c as there is no explicit integration along a curved path. However, the w field does contain downdrafts $< -3\,\mathrm{m\,s^{-1}}$ near the domain edges that appear unrealistic. Along the left domain edge, these increased downdrafts occur in the same location as in the coplane analysis (Fig. 12c).

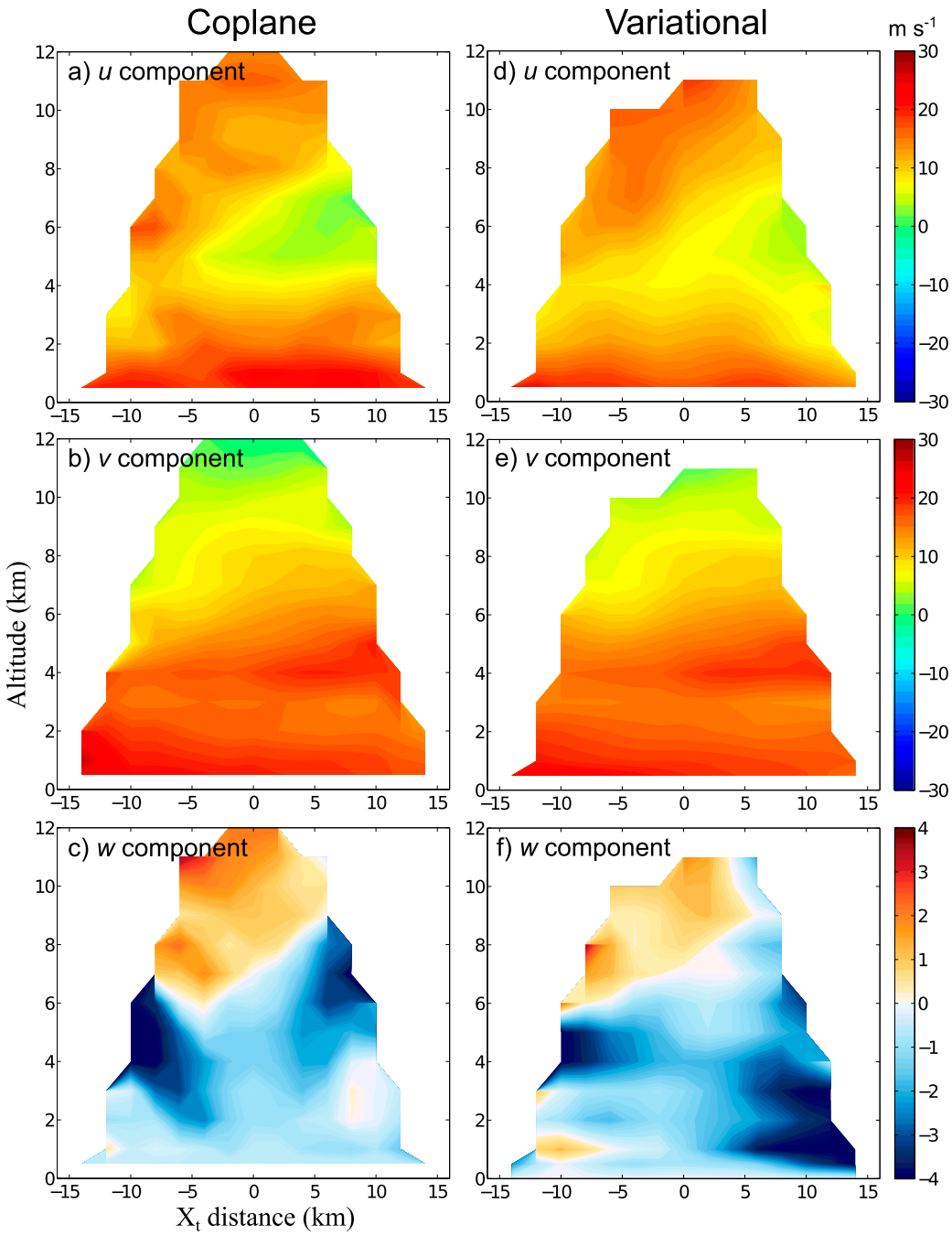

FIG. 12. Cross-track view of the (a) u, (b) v, and (c) w wind components as derived by the coplane analysis of the HIWRAP observations. (d)–(f) The variational analysis wind components. This cross section is taken at Y_t = 160 km from Fig. 11.

Along the right domain edge, these increased downdrafts are prominent in the lower altitudes and appear to trail off into the higher altitudes. This pattern of vertically oriented anomalies along the domain edge is reminiscent of the error pattern in Fig. 9f, which suggests that these features contain likely errors. The source of these errors cannot be traced to specific observations, but rather the errors must be attributed to the general decreased accuracy of the global solver along the domain edges.

Both the coplane and variational methods produced adequate wind fields that generally agreed well with each other. Both fields also contained inevitable localized errors. With a priori knowledge of the error patterns expected from each method, the questionable features

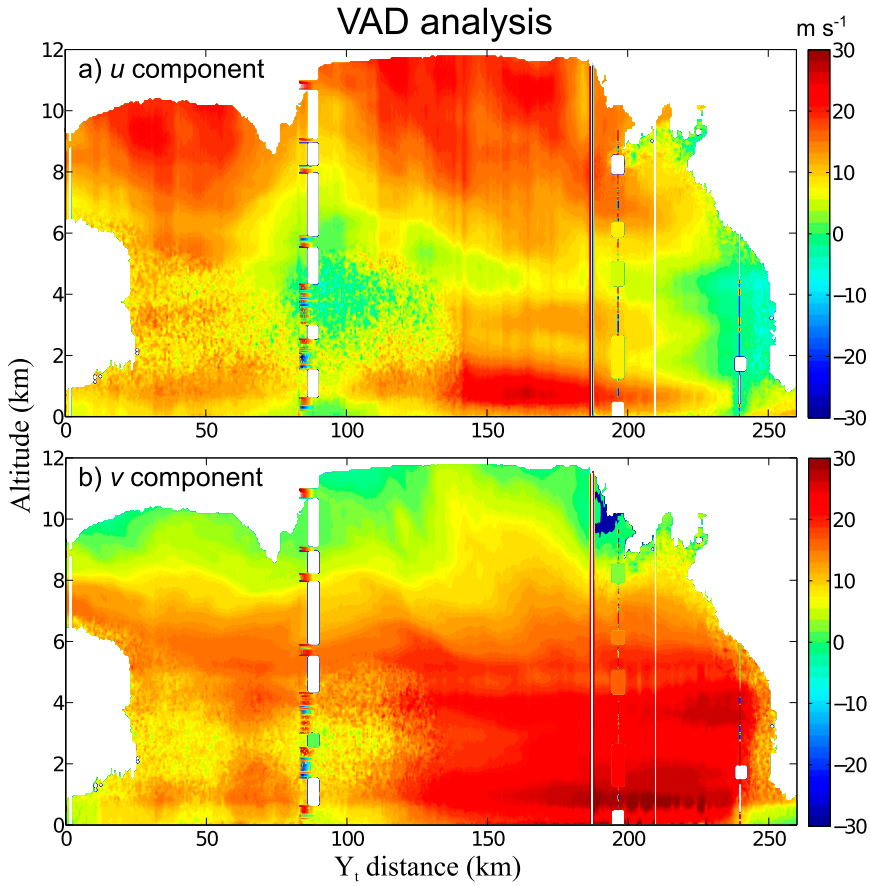

FIG. 13. Nadir view of the (a) u and (b) v wind components as derived by the VAD analysis of the HIWRAP observations seen in Fig. 6.

that appear in the solutions can be easily identified as retrieval errors. Identifying and understanding these errors is essential for reliable scientific interpretations of solutions from either analysis method.

We make a final comparison of retrieval techniques with the VAD technique from Tian et al. (2013). The VAD technique obtains the mean horizontal wind within the nadir plane by fitting the measured radial winds within a scan circle onto a sinusoidal curve. Figure 13 shows the retrieved u and v components of the wind for the same leg of data from Hurricane Ingrid. The VAD technique captures the same overall wind pattern that was retrieved by the other retrieval techniques (Fig. 11). The most noticeable difference in Fig. 13 is the increased vertical resolution. Since the VAD technique does not retrieve the full three-dimensional wind field, it is computationally less expensive than both the coplane and variational methods; moreover, this allows the VAD technique to preserve the high vertical resolution of the HIWRAP beam.

In calculating the mean horizontal wind, the wind field is assumed to have linear horizontal velocity and constant hydrometeor vertical speed across the total scan circle. These assumptions tend to hold well in stratiform precipitation regions like that in the current dataset since these mesoscale regions contain weak vertical velocities and winds that vary slowly over horizontal distances. To capture convective-scale features, one of the three-dimensional wind retrieval methods must be used.

7. Conclusions

In this paper, the coplane method for dual-Doppler wind retrieval (Armijo 1969; Miller and Strauch 1974) is adapted to the downward-pointing conically scanning technique of the NASA HIWRAP airborne radar. The coplane method takes the radar observations and solves for the three-dimensional winds using a simple interpolation and integration approach. This approach locally solves for the wind field, which is in contrast to the global optimization (variational) method described by Guimond et al. (2014). To retrieve the unobserved wind component U_α at all points, observations must exist at all points in the domain. The main advantage of

the coplane method is the transparency of its calculations. The interpolation and solving processes are discretely and separately calculated, which allows for exact calculation of wavelength resolution and tracing of source data from the solution.

Simulated radar observations of a model hurricane were used to test the coplane method and compare to the variational method. The coplane method retrieved the wind field with small errors relative to the wind speed magnitudes. Compared to the variational method, the coplane method had lower errors in the cross-track component (u) and vertical component (w) fields, while the variational method had lower errors in the along-track component (v) field. For the coplane method, the accuracy of u relied on the accuracy of the U_α boundary initializations. Where U_α was initialized sufficiently well, u remained accurate across the span of the domain. Where U_α was not well initialized, errors in u propagated along the curved integration path, creating an easily recognizable error signature. The w component, which is also derived from U_α, produced errors at the domain edges along curved integration paths with insufficiently initialized U_α. The error patterns for the variational field were different, showing errors in u and w that grew toward the edges of the domain at all altitudes.

The coplane and variational methods were applied to HIWRAP observations collected during the NASA HS3 campaign. Both techniques produced errors in the retrieval that appeared in patterns similar to the errors in the simulated radar retrieval. Prior knowledge of the error patterns expected from each method allowed for this recognition of retrieval errors in the HS3 retrieval. As a local solver, the errors in the coplane analysis are easily traced to the certain observations and/or U_α initializations. Unlike the transparency of a local solver, the errors arrived at with the global solver cannot be explicitly traced to certain observations or calculations since the solution at a particular location depends on the solution everywhere. Additionally, since the coplane method employs the Barnes filter, the corresponding response function provides the exact minimum resolvable wavelength of the final solution. The minimum resolvable wavelength for the variational method cannot be exactly calculated since the interpolation filter and Laplacian smoother are constraints on the optimization rather than exact calculations.

The coplane technique's ability to transparently trace the exact calculations from the raw observations to the final solution is highly beneficial when making scientific interpretations. This ability is necessary to more adequately analyze small-scale features in tropical cyclones, such as rotating deep convection (Hendricks et al. 2004; Montgomery et al. 2006; Sanger et al. 2014). A key skill for radar analyses is being able to separate true meteorological signals from nonmeteorological signals such as noise or data contamination that has bypassed the data quality control process. Once a solution is obtained, quirky regions in the final solution can be ambiguous as to whether they are true representations of small-scale features. After easily pinpointing the raw observations that were used to create the solution, the user can better assess the reality of the observations taken, and corrections can subsequently be implemented or not implemented. In the variational method, these anomalous measurements would be smoothed and may impact the entire retrieval, which would either dilute the small-scale signal or incorporate erroneous data into the solution. The coplane method can prevent incorrect scientific interpretations of inherently wrong solutions or strengthen confidence in the conclusions based on the observations. Given the wind component error analyses for both retrieval methods, the option to trace solution calculations with the coplane analysis is provided to the user with minimal cost to the accuracy of the overall solution.

Future work will use the coplane analysis for scientific research of observations from the HS3 field campaign and other planned campaigns employing the HIWRAP radar. This technique can also be used to analyze tail Doppler radar data from tropical cyclones documented in peer-reviewed work (e.g., Marks and Houze 1984; Reasor et al. 2009; Houze et al. 2009; Bell and Montgomery 2010), as well as future field campaigns. In locations directly beneath the aircraft, the geometry of the tail Doppler radar observations is compatible with the coplane technique. These additional analyses would be especially useful here as these locations are particularly troublesome for capturing small-scale features with the global optimization technique.

Acknowledgments. We thank Matthew McLinden, Lihua Li, Martin Perrine, Jaime Cervantes, and Ed Zenker for their engineering support and data processing for the HIWRAP radar. We thank Shuyi Chen for providing the model output used in this study. We also thank the three anonymous reviewers of this manuscript. The first author conducted this research at the NASA Goddard Space Flight Center under the support of the NASA Postdoctoral Program conducted by the Oak Ridge Associated Universities.

REFERENCES

Armijo, L., 1969: A theory for the determination of wind and precipitation velocities with Doppler radars. *J. Atmos. Sci.,* **26,** 570–573, doi:10.1175/1520-0469(1969)026<0570:ATFTDO>2.0.CO;2.

Barnes, S. L., 1973: Mesoscale objective analysis using weighted time-series observations. NOAA Tech. Memo. ERL NSSL-62, National Severe Storms Laboratory, Norman, OK, 60 pp. [NTIS COM-73-10781.]

Bell, M. M., and M. T. Montgomery, 2010: Sheared deep vortical convection in pre-depression Hagupit during TCS08. *Geophys. Res. Lett.,* **37,** L06802, doi:10.1029/2009GL042313.

Bousquet, O., and M. Chong, 1998: A multiple-Doppler synthesis and continuity adjustment technique (MUSCAT) to recover wind components from Doppler radar measurements. *J. Atmos. Oceanic Technol.,* **15,** 343–359, doi:10.1175/1520-0426(1998)015<0343:AMDSAC>2.0.CO;2.

Braun, S. A., and Coauthors, 2013: NASA's Genesis and Rapid Intensification Processes (GRIP) field experiment. *Bull. Amer. Meteor. Soc.,* **94,** 345–363, doi:10.1175/BAMS-D-11-00232.1.

Browning, K. A., and R. Wexler, 1968: The determination of kinematic properties of a wind field using Doppler radar. *J. Appl. Meteor.,* **7,** 105–113, doi:10.1175/1520-0450(1968)007<0105:TDOKPO>2.0.CO;2.

Chong, M., and J. Testud, 1996: Three-dimensional air circulation in a squall line from airborne dual-beam Doppler radar data: A test of coplane methodology software. *J. Atmos. Oceanic Technol.,* **13,** 36–53, doi:10.1175/1520-0426(1996)013<0036:TDACIA>2.0.CO;2.

Dazhang, T., S. G. Geotis, R. E. Passarelli Jr., and A. L. Hansen, and C. L. Frush, 1984: Evaluation of an alternating-PRF method for extending the range of unambiguous Doppler velocity. Preprints, *22nd Conf. on Radar Meteorology,* Zurich, Switzerland, Amer. Meteor. Soc., 523–527.

Doviak, R. J., P. S. Ray, R. G. Strauch, and L. J. Miller, 1976: Error estimation in wind fields derived from dual-Doppler radar measurement. *J. Appl. Meteor.,* **15,** 868–878, doi:10.1175/1520-0450(1976)015<0868:EEIWFD>2.0.CO;2.

Gamache, J. F., 1997: Evaluation of a fully three-dimensional variational Doppler analysis technique. Preprints, *28th Conf. on Radar Meteorology,* Austin, TX, Amer. Meteor. Soc., 422–423.

——, F. D. Marks Jr., and F. Roux, 1995: Comparison of three airborne Doppler sampling techniques with airborne in situ wind observations in Hurricane Gustav (1990). *J. Atmos. Oceanic Technol.,* **12,** 171–181, doi:10.1175/1520-0426(1995)012<0171:COTADS>2.0.CO;2.

Gao, J., M. Xue, A. Shapiro, and K. K. Droegemeier, 1999: A variational method for the analysis of three-dimensional wind fields from two Doppler radars. *Mon. Wea. Rev.,* **127,** 2128–2142, doi:10.1175/1520-0493(1999)127<2128:AVMFTA>2.0.CO;2.

Guimond, S. R., L. Tian, G. M. Heymsfield, and S. J. Frasier, 2014: Wind retrieval algorithms for the IWRAP and HIWRAP airborne Doppler radars with application to hurricanes. *J. Atmos. Oceanic Technol.,* **31,** 1189–1215, doi:10.1175/JTECH-D-13-00140.1.

Hendricks, E. A., M. T. Montgomery, and C. A. Davis, 2004: The role of "vortical" hot towers in the formation of Tropical Cyclone Diana (1984). *J. Atmos. Sci.,* **61,** 1209–1232, doi:10.1175/1520-0469(2004)061<1209:TROVHT>2.0.CO;2.

Heymsfield, G. M., L. Tian, A. J. Heymsfield, L. Li, and S. Guimond, 2010: Characteristics of deep tropical and subtropical convection from nadir-viewing high-altitude airborne Doppler radar. *J. Atmos. Sci.,* **67,** 285–308, doi:10.1175/2009JAS3132.1.

Hildebrand, P. H., and Coauthors, 1996: The ELDORA/ASTRAIA airborne Doppler weather radar: High-resolution observations from TOGA COARE. *Bull. Amer. Meteor. Soc.,* **77,** 213–232, doi:10.1175/1520-0477(1996)077<0213:TEADWR>2.0.CO;2.

Houze, R. A., Jr., 1997: Stratiform precipitation in regions of convection: A meteorological paradox? *Bull. Amer. Meteor. Soc.,* **78,** 2179–2196, doi:10.1175/1520-0477(1997)078<2179:SPIROC>2.0.CO;2.

——, W.-C. Lee, and M. M. Bell, 2009: Convective contribution to the genesis of Hurricane Ophelia (2005). *Mon. Wea. Rev.,* **137,** 2778–2800, doi:10.1175/2009MWR2727.1.

Jordan, C. L., 1958: Mean soundings for the West Indies area. *J. Atmos. Sci.,* **15,** 91–97, doi:10.1175/1520-0469(1958)015<0091:MSFTWI>2.0.CO;2.

Jorgensen, D. P., 1984: Mesoscale and convective-scale characteristics of mature hurricanes. Part I: General observations by research aircraft. *J. Atmos. Sci.,* **41,** 1268–1285, doi:10.1175/1520-0469(1984)041<1268:MACSCO>2.0.CO;2.

——, and J. D. DuGranrut, 1991: A dual-beam technique for deriving wind fields from airborne Doppler radar. Preprints, *25th Int. Conf. on Radar Meteorology,* Paris, France, Amer. Meteor. Soc., 458–461.

——, P. H. Hildebrand, and C. L. Frush, 1983: Feasibility test of an airborne pulse-Doppler meteorological radar. *J. Climate Appl. Meteor.,* **22,** 744–757, doi:10.1175/1520-0450(1983)022<0744:FTOAAP>2.0.CO;2.

Klimowski, B. A., and J. D. Marwitz, 1992: The synthetic dual-Doppler analysis technique. *J. Atmos. Oceanic Technol.,* **9,** 728–745, doi:10.1175/1520-0426(1992)009<0728:TSDDAT>2.0.CO;2.

Koch, S. E., M. desJardins, and P. J. Kocin, 1983: An interactive Barnes objective map analysis scheme for use with satellite and conventional data. *J. Climate Appl. Meteor.,* **22,** 1487–1503, doi:10.1175/1520-0450(1983)022<1487:AIBOMA>2.0.CO;2.

Lee, W.-C., P. Dodge, F. D. Marks Jr., and P. H. Hildebrand, 1994: Mapping of airborne Doppler radar data. *J. Atmos. Oceanic Technol.,* **11,** 572–578, doi:10.1175/1520-0426(1994)011<0572:MOADRD>2.0.CO;2.

Lhermitte, R. M., 1971: Probing of atmospheric motion by airborne pulse-Doppler radar techniques. *J. Appl. Meteor.,* **10,** 234–246, doi:10.1175/1520-0450(1971)010<0234:POAMBA>2.0.CO;2.

——, and D. Atlas, 1961: Precipitation motion by pulse Doppler radar. Preprints, *Ninth Conf. on Weather Radar,* Norman, OK, Amer. Meteor. Soc., 218–223.

Li, L., G. Heymsfield, J. Carswell, D. Schaubert, M. McLinden, M. Vega, and M. Perrine, 2011: Development of the NASA High-Altitude Imaging Wind and Rain Airborne Profiler. Preprints, *IEEE Aerospace Conf.,* Big Sky, MT, Institute of Electrical and Electronics Engineers, Paper 6.0202, 7 pp, doi:10.1109/AERO.2011.5747415.

Marks, F. D., Jr., and R. A. Houze Jr., 1984: Airborne Doppler radar observations in Hurricane Debby. *Bull. Amer. Meteor. Soc.,* **65,** 569–582, doi:10.1175/1520-0477(1984)065<0569:ADROIH>2.0.CO;2.

Miller, L. J., and R. G. Strauch, 1974: A dual Doppler radar method for the determination of wind velocities within precipitating weather systems. *Remote Sens. Environ.,* **3,** 219–235, doi:10.1016/0034-4257(74)90044-3.

Mohr, C. G., L. J. Miller, R. L. Vaughan, and H. W. Frank, 1986: The merger of mesoscale datasets into a common Cartesian format for efficient and systematic analyses. *J. Atmos. Oceanic Technol.,* **3,** 143–161, doi:10.1175/1520-0426(1986)003<0143:TMOMDI>2.0.CO;2.

Montgomery, M. T., M. M. Bell, S. D. Aberson, and M. L. Black, 2006: Hurricane Isabel (2003): New insights into the physics of intense storms. Part I: Mean vortex structure and maximum intensity estimates. *Bull. Amer. Meteor. Soc.,* **87,** 1335–1347, doi:10.1175/BAMS-87-10-1335.

Reasor, P. D., M. D. Eastin, and J. F. Gamache, 2009: Rapidly intensifying Hurricane Guillermo (1997). Part I: Low-wavenumber structure and evolution. *Mon. Wea. Rev.,* **137,** 603–631, doi:10.1175/2008MWR2487.1.

Sanger, N. T., M. T. Montgomery, R. K. Smith, and M. M. Bell, 2014: An observational study of tropical cyclone spinup in Supertyphoon Jangmi from 24 to 27 September. *Mon. Wea. Rev.,* **142,** 3–28, doi:10.1175/MWR-D-12-00306.1.

Tian, L., G. Heymsfield, S. Guimond, and L. Li, 2013: VAD and dual-Doppler analysis of wind fields from HIWRAP observations during GRIP. *36th Conf. on Radar Meteorology,* Breckenridge, CO, Amer. Meteor. Soc., 212. [Available online at http://ams.confex.com/ams/36Radar/webprogram/Paper229079.html.]